Solar Physics
DOI: 10.1007/•••••-•••-•••-••••-•

Forbush Decrease Prediction Based on the Remote Solar Observations

M. Dumbović[1] · **B. Vršnak**[1] · **J. Čalogović**[1]

Abstract We employ remote observations of coronal mass ejections (CMEs) and the associated solar flares to forecast the CME-related Forbush decreases, *i.e.*, short-term depressions in the galactic cosmic-ray flux. The relationship between the Forbush effect at the Earth and remote observations of CMEs and associated solar flares is studied *via* a statistical analysis. Relationships between Forbush decrease magnitude and several CME/flare parameters was found, namely the initial CME speed, apparent width, source position, associated solar-flare class and the effect of successive-CME occurrence. Based on the statistical analysis, remote solar observations are employed for a Forbush-decrease forecast. For that purpose, an empirical probabilistic model is constructed that uses selected remote solar observations of CME and associated solar flare as an input, and gives expected Forbush-decrease magnitude range as an output. The forecast method is evaluated using several verification measures, indicating that as the forecast tends to be more specific it is less reliable, which is its main drawback. However, the advantages of the method are that it provides early prediction, and that the input is not necessarily spacecraft-dependent.

Keywords: Coronal Mass Ejections, Low Coronal Signatures; Cosmic Rays, Galactic

1. Introduction

Short-term depressions in the galactic cosmic ray (GCR) flux were first observed by Forbush (1937) and Hess and Demmelmair (1937) and termed "Forbush decreases" (FD). There are two types: one caused by corotating interaction regions (see, *e.g.*, Richardson, 2004) and the other caused by interplanetary counterparts of CMEs (ICMEs) and/or the shocks that they drive (see, *e.g.*, Cane, 2000 and Belov, 2009). ICME-related FDs are typically asymmetric, and they have duration of a few days, magnitude larger than the daily CR-flux variations, and an onset close to the arrival of an ICME. If an ICME is preceded by a shock/sheath region, a characteristic two-step FD is expected, the first

[1] Hvar Observatory, Faculty of Geodesy, University of Zagreb, Zagreb, Croatia; email: mdumbovic@geof.hr

step coming from the sheath, whereas the second depression is associated with the ejecta (for an overview on ICME-related FDs see, *e.g.*, Cane, 2000 and Richardson and Cane, 2010). However, two-step FDs are not very common and FDs generally show a diverse and complex structure, even in the case of single ICMEs (Jordan *et al.*, 2011).

The physical mechanism behind the modulation of cosmic rays can be described in general by a transport equation (Parker, 1965), which combines contributions from convection and adiabatic energy loss by a fast stream and enhanced drift and scattering properties of strong and fluctuating magnetic field. These effects were considered in several models trying to explain FDs (*e.g.* Le Roux and Potgieter, 1991; Cane, Richardson, and Wibberenz, 1995; Wibberenz, Cane, and Richardson, 1997; Wibberenz *et al.*, 1998; Krittinatham and Ruffolo, 2009; Kubo and Shimazu, 2010). Since the models are based on the interaction of charged particles with interplanetary shock/sheath region and/or ejecta, any implementation of such models for forecasting purposes would be dependent on the observed interplanetary ICME characteristics. There have been many observational studies as well, relating FD magnitude to ICME interplanetary properties such as magnetic-field strength and fluctuations, and ICME speed (see, *e.g.*, Chilingarian and Bostanjyan, 2010; Richardson and Cane, 2011; Dumbović *et al.*, 2012; Blanco *et al.*, 2013 and references therein). The good relationship between *in-situ* properties of ICMEs and FDs enables using real-time near-Earth *in-situ* measurements to forecast the ICME-related Forbush effect. However, given the current position of spacecraft providing such measurements, predictions can precede the FD event only about one hour in advance. Furthermore, a recent study by Thomas *et al.* (2015) provided strong evidence for the modulation of GCR flux by remote solar-wind structures, *i.e.* this indicates that Forbush decreases can even be produced remotely.

To obtain timely information on a Forbush decrease, a forecast method is needed that can derive interplanetary properties of ICMEs based on the remote solar observations of CMEs and associated solar phenomena (*e.g.* solar flares or EUV dimmings). Moreover, since FD magnitude is dependent on the magnetic field and speed of the ICME, these should be derived from the initial CME properties during the liftoff. However, neither the magnetic field nor CME initial speed are directly observable. Chertok *et al.* (2013) used the magnetic flux at the photospheric level beneath EUV dimmings and post-eruption arcades associated with CMEs as a measure of a CME magnetic field and obtained a good correlation with the FD magnitude. However, only a fraction of CMEs are associated with EUV dimmings and moreover, there are CMEs without any chromospheric or low coronal signatures (stealth CMEs, see, *e.g.*, Robbrecht, Patsourakos, and Vourlidas, 2009; Howard and Harrison, 2013 and references therein). Recent studies have shown that using white-light coronagraphic observations of CMEs can relate their properties to FD magnitudes. FD magnitude was found to be larger for faster CMEs (Blanco *et al.*, 2013; Belov *et al.*, 2014), CMEs with larger apparent width (Kumar and Badruddin, 2014; Belov *et al.*, 2014) and CMEs with greater mass (Belov *et al.*, 2014). In addition, Belov (2009) found that the sources of the largest Forbush effects are usually located in the central part of the visible solar disc. However, it should be noted that CME measurements suffer

from projection effects and can therefore be taken only as proxies of CME initial coditions. In addition, the relations between these observed CME properties and FDs are much weaker compared to ICME–FD relations.

2. Data and Method for Statistical Analysis

We aim to relate remote CME observational properties to FD magnitude and employ statistical relationships in forecasting. In the article by Dumbović *et al.* (2015) an analogous problem was considered, trying to statistically relate remote CME observational properties to geomagnetic-storm strength. Therefore, we use the same methodology here. By analogy with the geoeffectiveness of CMEs, as a measure of geomagnetic response we adopt the term GCR-effectiveness (used by Kumar and Badruddin, 2014) as a measure of the cosmic-ray response.

We use a sample of events listed by Dumbović *et al.* (2015) and supplement it with FD events. The original list contains 211 CMEs with associated solar flares and geomagnetic response measured by the Disturbance storm time (Dst) index. The list consists of various CME observational properties taken from the *Solar and Heliospheric Observatory* (SOHO) *Large Angle and Spectrometric Coronagraph* (LASCO) CME Catalog (Yashiro *et al.*, 2004: cdaw.gsfc.nasa.gov/CMElist/) and solar flare data taken from the National Oceanic and Atmospheric Administration (NOAA) X-ray solar flare list (ftp://ftp.ngdc.noaa.gov/STP/space-weather/solar-data/solar-features/solar-flares). Each CME/flare event in the list is associated with a Dst value and time (time of the reported/measured Dst anomaly). For each CME in the list there is also an "interaction parameter" describing the likelihood that the CME interacts with some other CME(s). It is derived using CME timing, width, and source position with respect to other "close" CMEs (for more details see Dumbović *et al.*, 2015). The interaction parameter $[i]$ is a discrete parameter that can have four different values, corresponding to four levels of "interaction probability":

$i = 1$: "SINGLE" (S) events – no interaction;
$i = 2$: "SINGLE?" (S?) events – interaction not likely;
$i = 3$: "TRAIN?" (T?) events – probable interaction;
$i = 4$ "TRAIN" (T) events – interaction highly probable.

For each event on the list we searched for a corresponding response in the relative pressure-corrected cosmic-ray (CR) count in the ground-based neutron monitor (NM) data taken from the *Space Physics Interactive Data Resource* (SPIDR, spidr.ngdc.noaa.gov/spidr/). We searched the time interval spanning 5 days before and 15 days after the reported Dst anomaly to find a response in the CR count (if there is one). To reduce the effect of daily variations we used the average of three to four different mid-latitude NM stations (depending on data availability) at different asymptotic longitudes, but of similar rigidity (Novosibirsk, Calgary, Kiel, and Magadan, with vertical cutoff rigidity 2.91 GV, 1.09 GV, 2.29 GV, and 2.10 GV, respectively; for method details see Dumbović *et al.*, 2011). This method reduces the daily variations, but does not remove

them completely. Therefore, a threshold of 1 % (comparable to the daily variation amplitude) is chosen to distinguish GCR-effective events. If a clear depression in the CR count with a magnitude >1 % (from the onset point to the time of maximum decrease) is observed around the reported Dst timing (*i.e.* the time of the minimum Dst is within the FD duration interval), the event is regarded as GCR-effective; otherwise it is not regarded as GCR-effective. Thus we treat small FDs (<1 %) in the same way as "missing" FDs (*i.e.* when there is no event because the CME did not arrive at the Earth). The CR counts were normalized to the CR count in the quiet period before any disturbance. In some cases, where two consecutive geomagnetic storms could be identified separately, but only one Forbush decrease is observed, the two events are merged into one event, which is then regarded as an interacting-CMEs event (interaction parameter, $i = 4$). In such cases the CMEs involved are treated as one event, characterized by the solar parameters of the fastest CME involved in the interaction and with the apparent width of the widest CME involved. This, in addition to data gaps for several events, resulted in a new list of 187 CME–flare–Dst–FD associations.

By analogy with the method used by Dumbović *et al.* (2015), FD magnitudes $[FD]$ were grouped into four different levels of GCR-effectiveness:

$FD < 1\,\%$ (not GCR-effective);
$1\% < FD < 3\,\%$ (moderately GCR-effective);
$3\% < FD < 6\,\%$ (strongly GCR-effective);
$FD > 6\,\%$ (intensively GCR-effective).

We focus on specific CME/flare parameters *viz.* the initial CME speeds and angular width, solar flare soft X-ray class and location, and interaction parameter. To relate these parameters to FD a statistical analysis was performed using FD-distributions as a statistical tool. The selected CME/flare parameters were also binned. For some parameters the binning was obvious (*e.g.* interaction parameter) as they are already discrete parameters. For continuous parameters, all of the bins have approximately the same number of events, therefore, these bins are not equidistant. The FD-distribution mean is then calculated, which can be correlated with the change in the mean value of the (discrete) CME/flare parameter. To support/substantiate our analysis we use the method of overlapping bins. With this method, in addition to the original binning, an alternative binning is used and the results for both are then compared. The benefit is twofold: firstly, if the alternative binning leads to the same results as the original binning, it contributes to the plausability of the results; secondly, in this way additional data points are obtained for the correlation of the FD-distribution mean and the mean value of the (discrete) CME/flare parameter. Both original and alternative bins, as well as the corresponding number of the events are given in Table 1.

3. Statistical Analysis

The first parameter analyzed is the CME apparent width. The events in our data set were first categorized into three different CME apparent width bins, following

Table 1. CME/flare parameters binning and corresponding number of events

CME/flare parameter	original bins		alternative bins	
	bin	Number of events	bin	Number of events
CME apparent width [w]	$< 120°$	56	$< 60°$	20
	$120° - 360°$	32	$60° - 100°$	22
	$360°$	99	$100° - 140°$	25
			$140° - 360°$	21
			$360°$	99
CME initial speed [v]	$400 - 650$ km s^{-1}	31		
	$650 - 800$ km s^{-1}	27	$400 - 700$ km s^{-1}	40
	$800 - 1000$ km s^{-1}	31	$700 - 1000$ km s^{-1}	49
	$1000 - 1200$ km s^{-1}	33	$1000 - 1500$ km s^{-1}	50
	$1200 - 1700$ km s^{-1}	34	> 1500 km s^{-1}	48
	> 1700 km s^{-1}	31		
CME/flare source position distance from the center of the solar disc [r]	< 0.35 R$_\odot$	28		
	$0.35 - 0.5$ R$_\odot$	30	< 0.45 R$_\odot$	49
	$0.5 - 0.6$ R$_\odot$	25	$0.45 - 0.65$ R$_\odot$	44
	$0.6 - 0.75$ R$_\odot$	34	$0.65 - 0.85$ R$_\odot$	41
	$0.75 - 0.9$ R$_\odot$	32	> 0.85 R$_\odot$	53
	> 0.9 R$_\odot$	38		
solar flare soft X-ray flux peak value [I]			$< 2.5 \cdot 10^{-6}$Wm^{-2}	28
	$< 10^{-5}$Wm^{-2}	84	$2.5 - 5 \cdot 10^{-6}$Wm^{-2}	33
	$10^{-5} - 10^{-4}$Wm^{-2}	67	$5 - 15 \cdot 10^{-6}$Wm^{-2}	34
	$> 10^{-4}$Wm^{-2}	36	$15 - 50 \cdot 10^{-6}$Wm^{-2}	34
			$50 - 150 \cdot 10^{-6}$Wm^{-2}	33
			$> 150 \cdot 10^{-6}$Wm^{-2}	25
interaction parameter [i]	$i = 1$	83	$i = 1$ & $i = 2$	108
	$i = 2$	25	$i = 2$ & $i = 3$	46
	$i = 3$	21	$i = 3$ & $i = 4$	79
	$i = 4$	58		

the categorization from the SOHO/LASCO CME catalog into non-halo, partial halo, and halo CMEs (original bins for w are defined in Table 1). Due to the fact that (possibly) interacting CMEs are regarded as one entity ("TRAIN" and "TRAIN?" events, see Section 2), these events were associated with the width of the widest CME involved in (possible) interaction. Using FD binning for GCR-effectiveness explained in Section 2, three FD distributions were made (Figure 1a–c). The mean of each distribution was calculated, as well as the average value of width within a certain range, to quantitatively examine changes in the FD distribution for different CME width ranges (presented by crosses in Figure 1d). The whole procedure was repeated with alternative binning, using the apparent widths listed in the SOHO/LASCO CME catalog (alternative bins for w are defined in Table 1). A linear-least-square fit to all of the data in Figure 1d (for both original and alternative bins) shows a strong correlation. However, large standard deviations can be seen, *i.e.* a large scatter of FD values is present

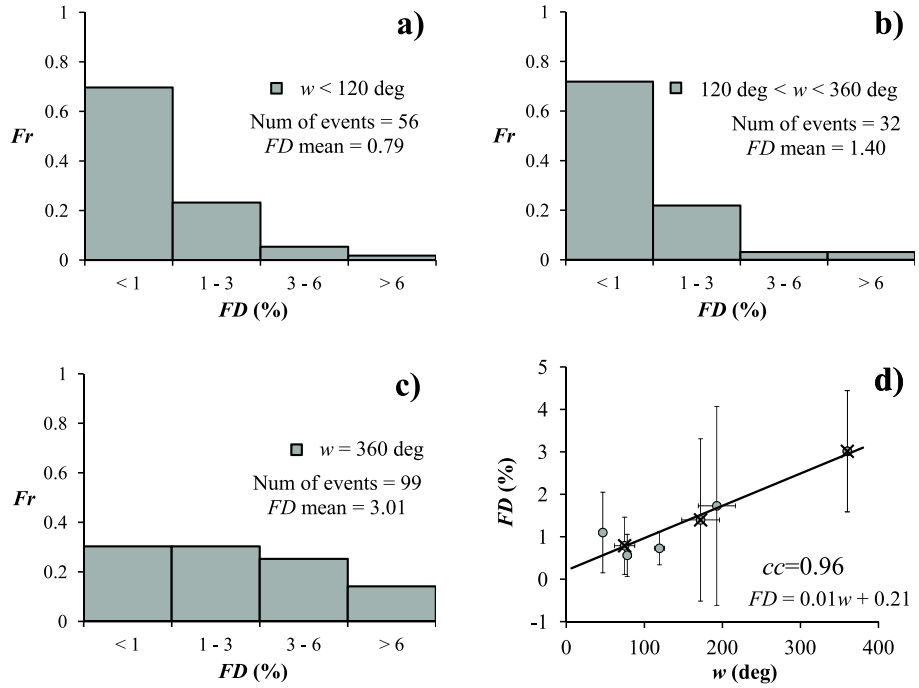

Figure 1. FD relative frequencies [Fr] for different FD and CME apparent-width [w] bins (a–c), and FD distribution mean as a function of the bin-averaged value for the CME apparent width (d). A linear fit to all of the data obtained by the method of overlapping bins is given in d with fitting parameters and a correlation coefficient [cc]. The data corresponding to original bins (used for distributions in a–c) are marked by crosses. Standard deviation is given by the error bars.

within each bin. This indicates that CMEs with larger apparent width are in general more GCR-effective, as concluded previously by Kumar and Badruddin (2014) and Belov *et al.* (2014), but there is a large event-to-event variability. We expect to observe this large variability for each of the solar parameters because although FD magnitude was observed to be related to some of the solar parameters, a strong correlation was not found (unless average values are used, as in Figure 1d). This implies a complex relation between the FD magnitude and a number of possible parameters, and therefore motivates a probabilistic approach.

Next, we analyze the first-order (linear) CME speed [v] derived from LASCO-C2 and -C3 images. The events in our data set were categorized into six different CME speed bins (original bins are listed in Table 1). For each category of v we obtain the GCR-effectiveness distribution, similarly as for apparent width [w]. For each distribution the distribution mean and corresponding average value of speed within a certain range is calculated (shown by crosses in Figure 2a). We again apply the method of overlapping bins (alternative bins are listed in Table 1). A linear-least-square fit to all of the data in Figure 2a (for both original and alternative bins) shows a strong correlation, indicating that FD magnitude is larger for faster CMEs, in agreement with Blanco *et al.* (2013) and Belov

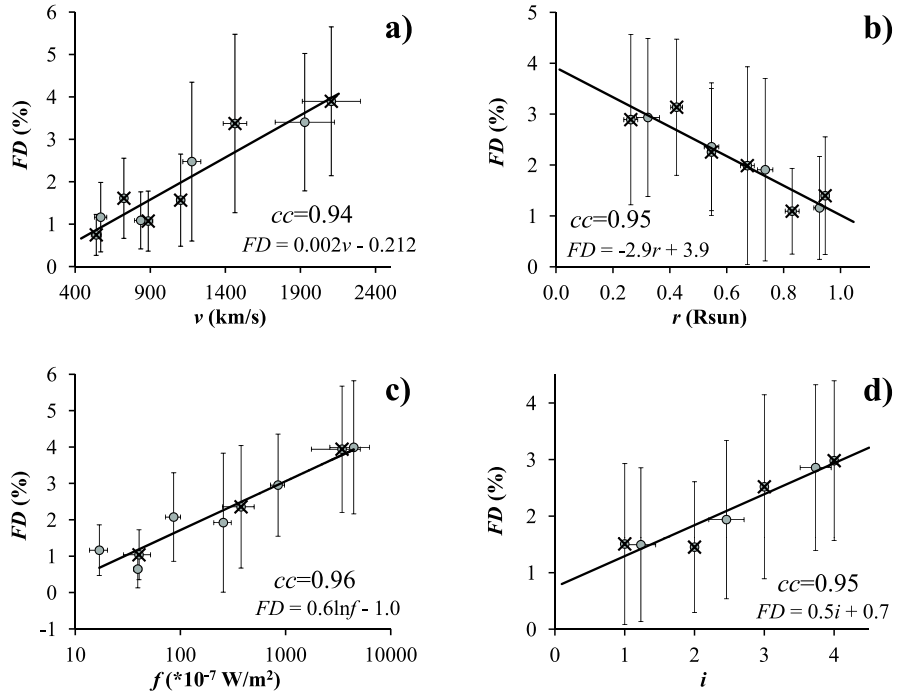

Figure 2. FD distribution mean as a function of the bin-averaged value for the CME initial speed [v] (a), CME/flare source position [r] (b), solar flare soft X-ray peak intensity (logarithmic scale) [f] (c), and CME–CME interaction level [i] (d). Best-fit to all of the data obtained by the method of overlapping bins is given for each of the solar parameter, as well as the corresponding fitting parameters and a correlation coefficient [cc]. The data corresponding to original bins are marked by crosses. Standard deviations are given by the error bars.

et al. (2014), although large standard deviations again imply large event-to-event variability.

Similar analysis, using the method of overlapping bins, was repeated for the CME/flare source position, *i.e.* for the radial distance of the CME/flare source position from the center of the solar disc, expressed in solar radii [r]. The first binning of r (shown by crosses in Figure 2b) contains six bins, whereas the alternative binning results in four bins (original and alternative bins for v are shown in Table 1). The linear-least-square fit to all of the data in Figure 2b results in a strong correlation, but with large standard deviations. Nevertheless, FD is found to be related to the CME/flare source position, namely it is found that FD is larger for CMEs/flares originating closer to the center of the solar disc, in agreement with Belov (2009).

FD magnitude was related to associated flare strength using the soft X-ray flux peak value [f] grouped according to the widely used classification of soft X-ray flares into B-, C-, M-, and X-class flares (original bins for [f] are shown in Table 1). Due to the small number of B-class flares, they share a bin with C-class flares. The alternative binning with six different ranges of soft X-ray flux peak value was applied, where each bin contains approximately the same number of

events (alternative bins for I are shown in Table 1). The best fit to all of the data obtained by the method of overlapping bins, in spite of the large standard deviations within bins, reveals a logarithmic dependence (Figure 2c), where FD is found to be larger for stronger flares.

Finally, we relate the FD magnitude [FD] to the CME–CME interaction parameter, which describes the likelihood that the CME will interact with another CME. As described in Section 2, this is a discrete, dimensionless parameter (original bins for i are shown in Table 1). For the purpose of the overlapping-bins method, alternative binning was applied, having three different bins, where events with close interaction parameter values were put in the same bin (*i.e.* bin 1 containing $i = 1$ and $i = 2$ events, bin 2 containing $i = 2$ and $i = 3$ events, bin 3 containing $i = 3$ and $i = 4$ events; see the alternative bins for i in Table 1). A linear-least-square fit to all of the data in Figure 2d (for both original and alternative bins) shows a strong correlation. As with all of the previous solar parameters, the standard deviations are again large within the bins. However, the results indicate that FD is generally related to the interaction parameter, *i.e.* that FD is larger for interacting/multiple CMEs.

4. Empirical Statistical Model for Predicting Forbush Decrease Magnitude

We use the results of the statistical analysis presented in the previous section to construct the distribution of FD magnitude for a specific set of remote solar observations of a CME and associated flare. The procedure is analogous to the one described by Dumbović *et al.* (2015).

As a mathematical tool we use the shifted geometric distribution (*i.e.* the geometric distribution for the random variable $Y = X - 1$, see, *e.g.*, Stirzaker, 2003):

$$P(X = k) = p(1 - p)^k \,, \tag{1}$$

where $P(X = k)$ is the probability that there will be k trials with a failure before the first trial with a success, and p is the probability of the success in each trial ($k = 0, 1, 2, ...$ is the number of trials). The shifted geometric distribution can easily be constructed if the distribution mean [m] is known:

$$p = \frac{1}{1 + m}, \tag{2}$$

where p is the probability of the success in each trial and m is the distribution mean.

For our sample, the following association is made between the number of trials, k and FD magnitude ranges:

- $k = 0 \longleftrightarrow FD < 1\,\%$;
- $k = 1 \longleftrightarrow 1\% < FD < 3\,\%$;
- $k = 2 \longleftrightarrow 3\% < FD < 6\,\%$;

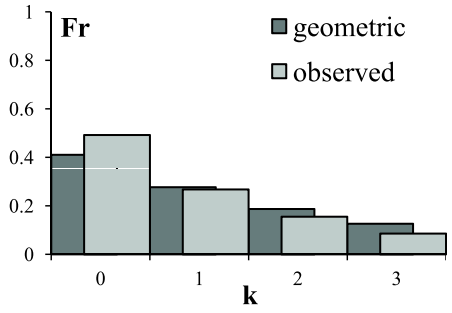

Figure 3: Comparison of the observed FD distribution and calculated geometric distribution (FD relative frequencies, F_r for different FD magnitude ranges, k) for the whole sample of 187 events.

- $k = 3 \longleftrightarrow FD > 6\,\%$.

Using $k \leftrightarrow FD$ association we obtain the relative frequency distribution of FD for our sample of 187 events (Figure 3). We calculate the distribution mean, $m = 2.07$, and then using Equations (1) and (2) with renormalization (so that the total probability on all trials equals one) we construct the shifted geometric distribution for the whole sample of 187 events. In Figure 3 we compare the distribution for our sample reconstructed using shifted geometric distribution to the observed distribution and a good agreement can be seen. A similar distribution of the observed FDs was obtained by Belov (2009).

Since our sample in general follows the shifted geometric distribution, we assume that the shifted geometric distribution can describe the probability distribution of FD magnitude $[FD]$ for a *certain* event with a specific set of remote solar observations of a CME and the associated flare. It was shown in Figures 1 and 2 that the trend of the change in the FD distribution mean with a specific solar parameter can be fitted by a corresponding function. Therefore, based on the relationships found between FD and solar parameters, a corresponding shifted geometric distribution can be obtained using Equations (1) and (2) for each solar parameter. We treat the empirical distribution obtained as a probability distribution for a specific solar parameter α, where $\alpha = v, w, r, f, i$ (*i.e.* initial CME speed $[v]$, CME apparent width $[w]$, CME/flare source position distance from the center of the solar disc $[r]$, flare strength $[f]$, and interaction parameter $[i]$). The probability distribution for a specific parameter provides the information on the probability for associating it with a specific value of k, *i.e.* FD magnitude range. To combine the effect of solar parameters, they were treated as mutually non-exclusive and independent, in which case a joint probability distribution is given by Dumbović *et al.* (2015):

$$\begin{aligned} P(FD=k) = \sum_{\alpha} P_\alpha - \sum_{\alpha\neq\beta} P_\alpha P_\beta + \sum_{\alpha\neq\beta\neq\gamma} P_\alpha P_\beta P_\gamma - \\ - \sum_{\alpha\neq\beta\neq\gamma\neq\delta} P_\alpha P_\beta P_\gamma P_\delta + \sum_{\alpha\neq\beta\neq\gamma\neq\delta\neq\epsilon} P_\alpha P_\beta P_\gamma P_\delta P_\epsilon \,, \end{aligned} \tag{3}$$

where $P_\alpha{=}P(\alpha)$ represents the probability of a specific FD magnitude range ($FD \leftrightarrow k$) for a specific solar parameter α.

Table 2. CME/flare input parameters [α] and corresponding calculated geometric distribution parameters [$m(\alpha)$ and $p(\alpha)$] for two extreme events

EVENT 1			EVENT 2		
α	$m(\alpha)$	$p(\alpha)$	α	$m(\alpha)$	$p(\alpha)$
$v = 2000$ km s^{-1}	3.79	0.2089	$v = 450$ km s^{-1}	0.69	0.5924
$w = 360°$	3.81	0.2079	$w = 50°$	0.71	0.5848
$r = 0.05$ R$_\odot$	3.76	0.2103	$r = 0.99$ R$_\odot$	1.03	0.4929
$f = 5000\text{x}10^{-7}$ W m^{-2}	4.11	0.1957	$f = 10\text{x}10^{-7}$ W m^{-2}	0.38	0.7238
$i = 4$	2.70	0.2703	$i = 1$	1.20	0.4545

Using the found relationships between FD and solar parameters from Figures 1 and 2, and Equations (1) – (3) we calculate a probability distribution for two extreme events: EVENT 1, which was a very fast and wide CME, involved in a CME–CME interaction and associated with a strong X-class flare close to the center of the solar disc (presumably intensly GCR-effective), and EVENT 2, which was a slow and narrow CME, which was not involved in a CME–CME interaction and is associated with a weak B-class flare near the limb of the solar disc (presumably not GCR-effective). The input CME/flare parameters for both of these extreme events is given in Columns 1 and 3 in Table 2, respectively. Using the relationships between FD and solar parameters from Figures 1 and 2 (suitable for the given units), we obtain the distribution mean for each of the solar parameters [$m(\alpha)$] (Columns 2 and 4 in Table 2). It can be seen that $m(\alpha)$ attains smaller values for EVENT 2, as expected (the distribution is shifted towards smaller FD magnitudes). Using Equation (2), we obtain the corresponding probability of success in each trial for each of the solar parameters, [$p(\alpha)$] (Columns 3 and 6 in Table 2), where the shift of the FD distribution for the EVENT 2 towards smaller FD magnitudes is reflected by the increased values of $p(\alpha)$.

Using Equation (1) the relative frequency for each trial [$k = 0, 1, 2, 3$] and each solar parameter [$\alpha = v, w, r, f, i$] can be calculated for each of the two extreme events. Finally, using Equation (3), we calculte the joint probability distribution, *i.e.* the relative frequency for a given set of solar parameters [v, w, r, f, i] for each trial [k] and renormalize it so that the total probability equals one ($\sum_{k=0}^{3} P(k) = 1$). The resulting distribution represents the joint probability distribution of observing FD magnitude [FD] in a specific range [$FD < 1\,\%$, $1\,\% < FD < 3\,\%$, $3\,\% < FD < 6\,\%$, $FD > 6\,\% \leftrightarrow k = 0$, $k = 1$, $k = 2$, $k = 3$] for a CME/flare event with a specific set of solar parameters [v, w, r, f, i]. The joint probability distributions for EVENT 1 and EVENT 2 are shown in Figure 4.

It can be seen in Figure 4 that the distribution for the two extreme events is different and that the probability for higher FD magnitudes is larger for EVENT 1, representing faster and wider CMEs that originate near the disc center, are related to more energetic flares and are likely to be involved in a CME-CME interaction. However, in both distributions the highest probability is that the event will not be GCR-effective, *i.e.* that FD magnitude will be $FD < 1\,\%$ ($k = 0$). Although the probability distribution changes with CME/flare parameters it is always highly asymmetric with the greatest probability that CME will not be

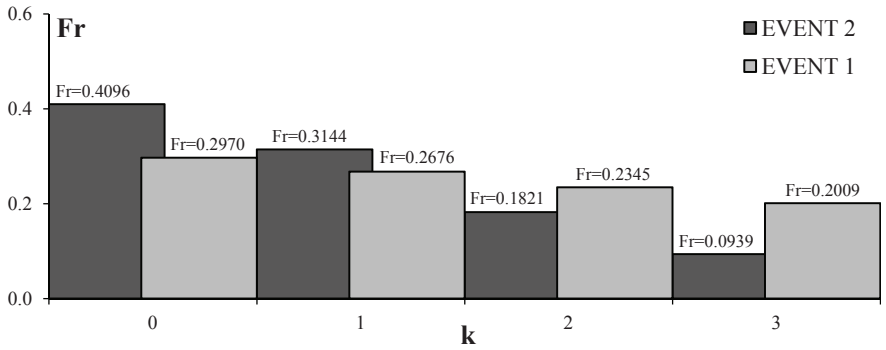

Figure 4. The joint probability distribution for EVENT 1 (light grey) and EVENT 2 (dark grey). The values of relative frequencies are given above the corresponding k-bin.

GCR-effective. This depicts the general behavior of CMEs seen in Figure 3: a large majority of CMEs will never reach the Earth and/or will not be very GCR-effective. Therefore, the probability distribution does not give a straightforward prediction of whether or not (and how large) Forbush decrease will be. Therefore, the level of GCR-effectiveness needs to be obtained by imposing some criteria (thresholds) on the probability distribution.

In Figure 4 we can see that for low GCR-effectiveness (EVENT 2) we expect a much higher value of relative frequency for $k = 0$ $[F_r(k = 0)]$ than for the highly GCR-effective event (EVENT 1). Conversely, we expect a much higher value of relative frequency for $k = 3$ $[F_r(k = 3)]$ for a highly GCR-effective event (EVENT 1), than for a low GCR-effectiveness (EVENT 2). Therefore, thresholds on the value of the relative frequency for a certain bin can be established to enclose a certain range of GCR-effectiveness. These thresholds are derived empirically. For that purpose we use the list of 187 CME–flare–Dst–FD associations and calculate FD magnitude distribution for each of the events in the list, based on the corresponding CME/flare parameters. Therefore, for each event we obtain four different relative frequency values $[F_r(k)]$ corresponding to four different distribution bins: $k = 0, 1, 2, 3$. For each relative frequency $[F_r(k)]$ we produce a scatter plot against the observed FD value, where FD is expressed as one of the four possible FD magnitude ranges associated with four different k: $[FD < 1\,\%$, $1\,\% < FD < 3\,\%$, $3\,\% < FD < 6\,\%$, $FD > 6\,\% \leftrightarrow k = 0$, $k = 1$, $k = 2$, $k = 3]$. Since FD is given by four discrete values, the data in these plots will be scattered in four lines at $k = 0, 1, 2, 3$. Each of the lines contains a number of data points that corresponds to the number of observations of different FD magnitude range (92 events with $k = 0$, 50 events with $k = 1$, 29 events with $k = 2$, and 16 events with $k = 3$). We find it useful to present the scatter plot for each of these four lines as a density plot using percentiles. In that way, it is noticeable how many data points are encompassed in each $F_r(k)$. Using the density of data scatter as a guideline, we derive thresholds T1 – T5 as values which best separate different GCR-effectiveness. These density plots representing the data scatter of the calculated relative requencies $[F_r(k)]$ against the observed FD magnitude, as well as thresholds T1 – T5, are presented in Figure 5.

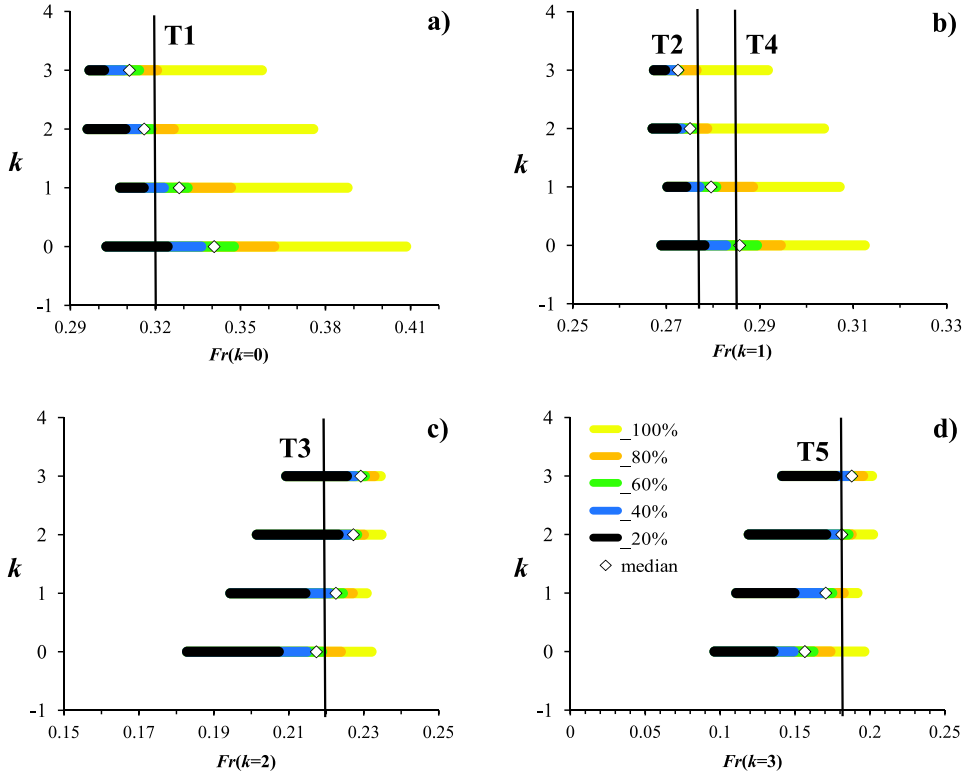

Figure 5. Density plots representing data scatter of the calculated relative frequencies $[F_r(k)]$ against the observed FD magnitude ranges $[k]$ for 187 CME–flare–Dst–FD associations. The density of the data points is expressed by differently colored percentiles. White diamond marks median, whereas black lines mark established thresholds T1 – T5 (for explanation see main text).

It can be seen in Figure 5a that almost 80 % of $k = 3$ events and 60 % of $k = 2$ events have $F_r(k = 0) < 0.32 \equiv T1$, whereas more than 80 % of non GCR-effective events ($k = 0$) and more than 60 % of moderately GCR-effective events ($k = 1$) have $F_r(k = 0) > T1$. Therefore, we establish $T1$ as a threshold separating $k = 0, 1$ events from $k = 2, 3$ events. Similarly, we obtain thresholds $T2$ and $T3$ in Figures 5b and 5c, respectively. Establishing a threshold between $k = 0$ and $k = 1$ events is more challenging, since the difference in the data density is less pronounced compared to separating $k = 0, 1$ and $k = 2, 3$ events. In Figure 5b a threshold $T4$ is shown, which separates $k = 0$ data (more than 50 % of events have $F_r(k = 1) > T4$) from $k = 1$ data (more than 60 % of events have $F_r(k = 1) < T4$). The difference in the data density is even less pronounced in separating $k = 2$ and $k = 3$ events. In Figure 5d a threshold $T5$ is shown, which separates $k = 2$ data (more than 50 % of events have $F_r(k = 3) < T5$) from $k = 3$ data (more than 50 % of events have $F_r(k = 3) > T5$).

We interpret the thresholds as values that encompass most of the events with a certain GCR-effectiveness. For example, most of the intense GCR-effective

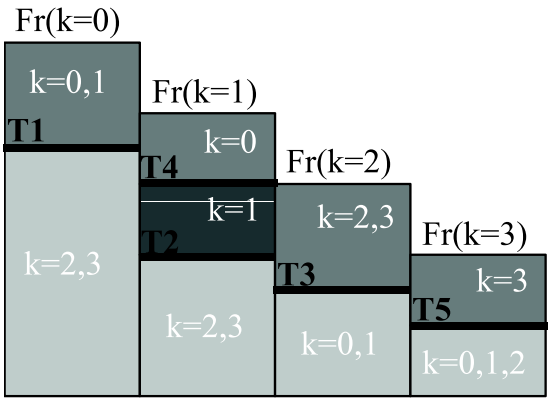

Figure 6: Schematic of thresholds for relative frequencies of certain bins $F_r(k)$: $T_1 = 0.32$, $T_2 = 0.277$, $T_3 = 0.222$, $T_4 = 0.285$, and $T_5 = 0.183$. Possible GCR-effectiveness level k is given for values above/below the corresponding threshold.

events ($FD > 6\,\% \leftrightarrow k = 3$) have a relative frequency for $k = 3$, $F_r(k = 3) > T5$. Therefore, we expect that if $F_r(k = 3) < T5$ the event will be intensly GCR-effective ($FD > 6\,\% \leftrightarrow k = 3$), otherwise it will be less GCR-effective, *i.e.* it will have some other level of GCR-effectiveness: $\{FD < 1\,\%,\ 1\,\% < FD < 3\,\%,\ 3\,\% < FD < 6\,\%\} \leftrightarrow \{k = 0,\ k = 1,\ k = 2\}$. A schematic of the thresholds for relative frequencies of certain bins is given in Figure 6. Conditions for some of the thresholds immediately give the information on which GCR-effectiveness level is expected. However, for some thresholds there still remains a set of possible GCR-effectiveness levels. Combining conditions for different thresholds, a unique GCR-effectiveness level can be obtained. The conditions for determing the GCR-effectiveness level using thresholds are given in Table 3.

For example, when we apply the first three conditions from Table 3 to the joint probability distribution for EVENT 1 (Figure 4) we derive the following: $F_r(k = 3) > T_1$, $F_r(k = 2) > T_2$, and $F_r(k = 0) < T_3$. All three conditions are in favor of $k = 2, 3$; therefore we apply the final condition from Table 3 and find that $F_r(k = 1) < T_5$, which means that the expected FD magnitude is $k = 3 \leftrightarrow FD > 6\,\%$. We repeat the calculation for EVENT 2 from Figure 4, where the first three conditions from Table 3 result in $F_r(k = 3) < T_1$, $F_r(k = 2) < T_2$, and $F_r(k = 0) > T_3$ being in favor of $k = 0, 1$. We then apply the fourth condition from Table 3 and find that $F_r(k = 1) > T_4$, which means that the expected FD magnitude is $k = 0 \leftrightarrow FD < 1\,\%$. Therefore, starting from extremely different solar CME/flare parameters we derive two extremes of GCR-effectiveness level (EVENT 1 is intensly GCR-effective, whereas EVENT 2 is not GCR-effective).

The model is empirical and based on the remote solar CME/flare observations of the sample used; therefore, the model input has certain limitations. CME speed $[v]$ is a continuous parameter given in units $\mathrm{km\,s^{-1}}$ in the range $v > 106$, restricted by the v-intercept in Figure 2a. The CME/flare source distance from the center of the solar disc $[r]$ is also a continuous parameter given in units of solar radii, with the range restricted by the physical boundaries, $0 \leq r \leq 1$ (*i.e.* the center of the solar disc and the solar limb). The apparent width $[w]$ is a continuous parameter restricted to the range $0^\circ < w \leq 360^\circ$, determined by

Table 3. The conditions for determing the GCR-effectiveness level using thresholds $[T_i,\ i = 1, 2, 3, 4, 5]$ for relative frequencies of certain bins $[F_r(k)]$ given in Figure 5. Combination of these conditions give a unique GCR-effectiveness level.

condition based on thresholds	result (if satisfied)	result (if not satisfied)	description of the conditions
$F_r(k=3) < T_1$	$k = 0, 1$	$k = 2, 3$	the combination of the first
$F_r(k=2) < T_2$	$k = 0, 1$	$k = 2, 3$	three conditions determines
$F_r(k=0) > T_3$	$k = 0, 1$	$k = 2, 3$	whether $k = 0, 1$ or $k = 2, 3$
$F_r(k=1) > T_4$	$k = 0$	$k = 1$	once established that $k = 0, 1$ this condition determines whether $k = 0$ or $k = 1$
$F_r(k=1) > T_5$	$k = 2$	$k = 3$	once established that $k = 2, 3$ this condition determines whether $k = 2$ or $k = 3$

observational boundaries ($w = 0°$ means a CME was not detected, $w = 360°$ is a halo CME). The flare strength parameter $[f]$, *i.e.* flare soft X-ray peak intensity, is a continuous parameter $[10^{-7}\mathrm{W\,m^{-2}}]$ in the range $f > 5.3$ restricted by the f-intercept in Figure 2c. Finally, the interaction parameter $[i]$ is a discrete parameter that can attain values $i = 1, 2, 3, 4$ based on the likeliness of the CME–CME interaction (Section 2).

Finally, we consider the implications of the approximation, where the solar parameters were treated as independent and Equation (3) applies. As noted by Dumbović *et al.* (2015) this assumption is not fully valid, due to the fact that not all key solar parameters are independent of each other and this assumption may increase to some extent the number of false alarms. However, we note that this assumption substantially simplifies the calculation of the joint probability, while on the other hand, the number of the false alarms is greatly influenced by the fact that the probability distribution is highly asymmetrical and in favor of low GCR-effectiveness, and even the optimized thresholds do not enclose *all* of the events (only a majority of events).

5. Evaluation of the Prediction

The prediction was evaluated first using the **training set**, *i.e.* the sample of the 187 CME–flare–FD associations used for the statistical analysis. The evaluation applied to the training set describes the successfulness and the reliability of the prediction model with respect to the approximations used, since we assume that our sample represents the ensemble of possibilities for a certain event. Next we perform the evaluation using a **test set**, *i.e.* independent sample of additionally selected and measured 42 CME–flare–FD events. We note that the two sets are conveniently named in analogy with the neural network approach (see, *e.g.*, Valach *et al.*, 2009; Uwamahoro, McKinnell, and Habarulema, 2012;

Table 4. Contingency table for a binary event

		Observation	
		YES	NO
Forecast	YES	a = number of hits, *i.e.* correctly forecasted events	b = number of false alarms, *i.e.* forecasts of an event while no event was observed
	NO	c = number of misses, *i.e.* events which were not forecasted	d = number of correct rejections, *i.e.* events which were not forecasted while indeed no event was observed

Sudar, Vršnak, and Dumbović, 2015), which typically uses three different sets (training set, validating set, and test set), with the difference that in our case the validating set is identical to the training set. The test set comprises of events in the time period 1998 – 2012, which are not present in the training set. The method for FD association is the same as for the training set (described in Section 2), with the difference that the CR data after 2011 were taken from the Neutron Monitor Database event search tool (www.nmdb.eu/nest/search.php) from Kiel, Magadan, and Newkirk stations.

We evaluate the forecast by comparing the predicted value with the observed value using verification measures for binary events (see, *e.g.*, Devos, Verbeeck, and Robbrecht, 2014). The verification measures are defined based on the contingency table (Table 4), which describes four possible outcomes (hit, false alarm, miss, and correct rejection). For the purpose of the evaluation we redefine the "event" as association of FD with a particular value. For example we define $k = 0$ ($FD < 1\,\%$) as an event. The event is classified as a "hit" when $k = 0$ was both observed and predicted; "false alarm" is when $k = 0$ is observed, while $k \neq 0$ was predicted; "miss" is when $k \neq 0$ was observed, while $k = 0$ was predicted; "correct rejection" is when $k \neq 0$ was both observed and predicted.

We use the following verification measures (for more details see Devos, Verbeeck, and Robbrecht, 2014 and references therein):
The Probability Of Detection (POD) or hit rate, the ratio of the number of hits and the number of events, calculated as POD= $a/(a + c)$;
The False Alarm Ratio (FAR), the ratio of the number of false alarms and the total number of forecasts, calculated as FAR=$b/(a + b)$;
Bias (BIAS), the ratio of the number of forecasts of occurrence to the number of actual occurrences, calculated as BIAS=$(a + b)/(a + c)$;
Heidke Skill Score (HSS), skill score taking into account the number of correct random forecasts, calculated as HSS=$(a + d - E)/(n - E)$,
where $E = ((a + c)(a + b) + (c + d)(b + d))/n$ and $n = a + b + c + d$

Each of the verification measures gives information on the quality of the prediction, however, none of them gives a full information on the quality of the forecast system. POD describes what fraction of the observed "yes" events were correctly forecast and ranges from 0 to 1, with perfect score POD = 1 (all hits). It is sensitive to hits, but ignores false alarms and therefore should be used in conjunction with FAR. FAR describes how many of the predicted "yes" events were false alarms, however, it ignores misses and consequently has to be used

Table 5. The number of possible outcomes based on the contingency table and the corresponding verification measures for validation and test sets, for different events

	event	a	b	c	d	POD	FAR	BIAS	HSS
training set	$k=0$	45	22	34	86	0.57	0.33	0.85	0.37
	$k=1$	21	34	42	90	0.33	0.62	0.87	0.06
	$k=2$	8	25	21	133	0.28	0.76	1.14	0.11
	$k=3$	10	22	6	149	0.63	0.69	2.00	0.34
	$k<3$	149	6	22	10	0.87	0.04	0.91	0.34
	$k<2$	110	12	32	33	0.77	0.10	0.86	0.44
	$k>0$	86	34	22	45	0.80	0.28	1.11	0.37
test set	$k=0$	8	6	9	19	0.47	0.43	0.82	0.24
	$k=1$	3	11	4	24	0.43	0.79	2.00	0.08
	$k=2$	3	4	8	27	0.27	0.57	0.64	0.16
	$k=3$	3	4	4	31	0.43	0.57	1.00	0.31
	$k<3$	31	4	4	3	0.89	0.11	1.00	0.31
	$k<2$	21	7	3	11	0.88	0.25	1.17	0.50
	$k>0$	19	9	6	8	0.76	0.32	1.12	0.24

in conjunction with POD. It ranges from 0 to 1, with perfect score FAR = 0 (no false alarms). BIAS measures the ratio of the frequency of forecasts to the frequency of observations and ranges from 0 to ∞, with perfect score BIAS = 1. It reveals whether the forecast has a tendency to underforecast (BIAS<1) or overforecast (BIAS>1) events. However, it tells nothing about how well the forecast corresponds to the observations. Finally, HSS estimates the accuracy of the forecast relative to that of random chance. It ranges from -∞ to 1, where HSS = 1 is a perfect score, HSS = 0 means that the forecast is no better than random, and HSS<0 means that the forecast is worse than random. The number of possible outcomes based on the contingency table, as well as the corresponding verification measures for both the training and the test set, are given in Table 5 for the following "events": $k = 0$ ($|FD| < 1\,\%$), $k = 1$ ($1\,\% < |FD| < 3\,\%$), $k = 2$ ($3\,\% < |FD| < 6\,\%$), $k = 3$ ($|FD| > 6\,\%$), $k = 0, 1, 2$ ($|FD| < 6\,\%$), $k = 0, 1$ ($|FD| < 3\,\%$), $k = 1, 2, 3$ ($|FD| > 1\,\%$). We note that the first four "events" correspond to the four bins of the probability distribution in Sections 3 and 4, whereas the last three "events" represent a less specific forecast. For these two groups of events verification measures are also presented separately in Figure 7 for the training and test sets.

It can be seen from Table 5 and Figure 7 that there are differences in the verification measures between the training and test sets, especially for the BIAS in case of a more specific forecast (*i.e.* for the forecast of a specific bin [$k = 0, 1, 2, 3$]). However, the differences are not pronounced and moreover they are not systematic, indicating that the successfulness of the forecast mainly relies on the approximations used and not the sample. The forecast of the intermediate bins $k = 1, 2$ is least reliable, since we get the lowest number of hits and largest number of false alarms. This is also evident in the HSS, which gives lowest values indicating that the forecast is only slightly better than random for these

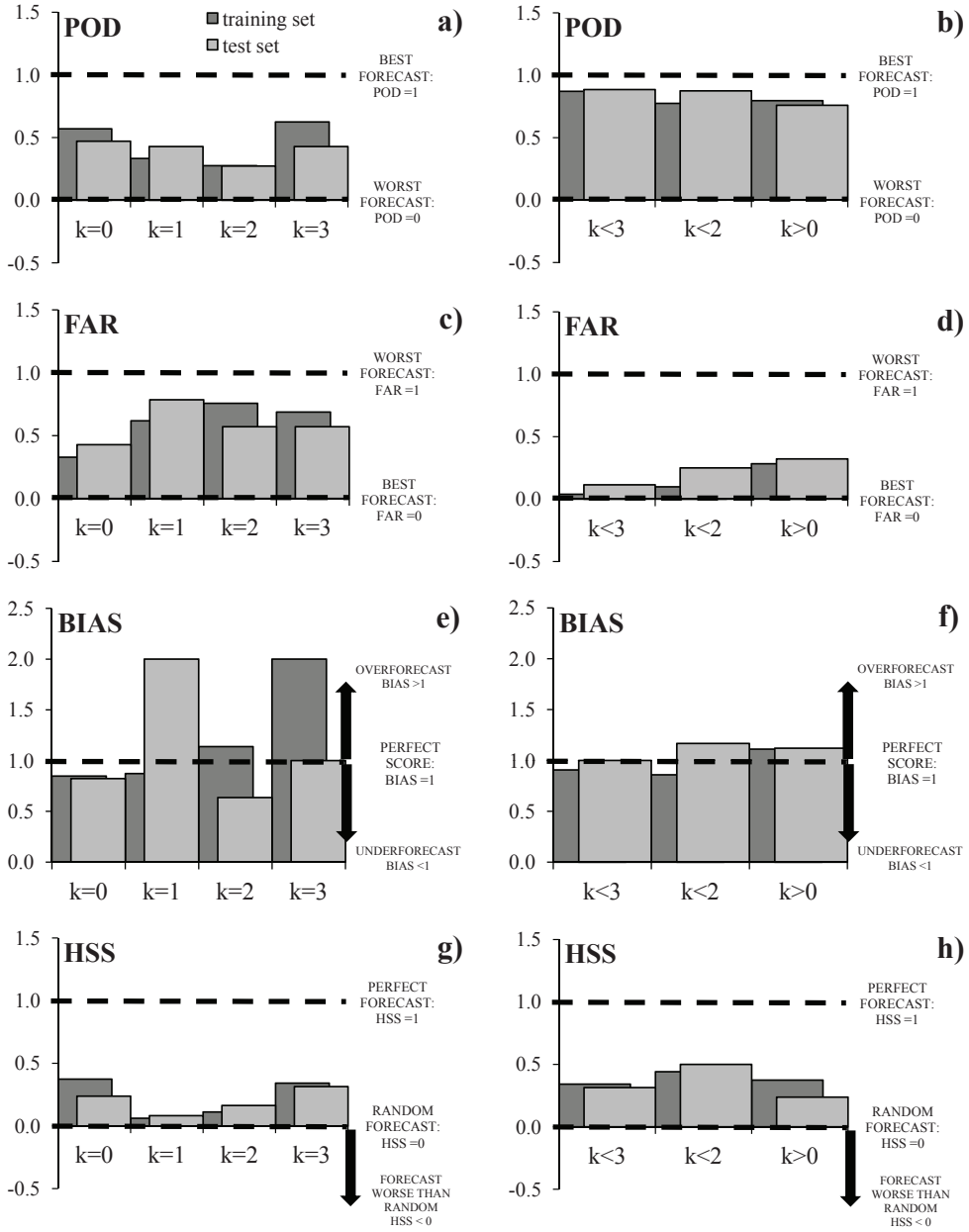

Figure 7. The Probability Of Detection (POD), False Alarm Ratio (FAR), BIAS, and Heidke Skill Score (HSS) for training and test sets for a more specific ($[k = 0, 1, 2, 3]$) and less specific ($[k < 3$, $k < 2$, and $k > 0]$) forecast.

two bins. This indicates that the forecast has a "resolution" problem, *i.e.* it has difficulties in discerning between neighboring bins. This is also supported by the fact that when less specific bins are regarded ($k < 3$, $k < 2$, and $k > 0$), POD is much higher, FAR is lower, BIAS is closer to perfect value (BIAS$\approx$ 1) and HSS has larger positive values, the latter indicating that the forecast shows skill compared to random forecast (see Table 5 and Figures 7c and 7d). Therefore, we conclude that the Forbush decrease prediction is more reliable for a less specific forecast, *i.e.* for predicting whether or not CME will be GCR-effective ($k > 0 \leftrightarrow FD > 1\,\%$), whether or not it will be strongly/intensly GCR-effective ($k < 2 \leftrightarrow FD < 3\,\%$) and whether or not it will be intensly GCR-effective ($k < 3 \leftrightarrow FD < 6\,\%$). Given the verification measures presented in Table 5 and Figure 7, the most reliable forecast (highest POD, lowest FAR, BIAS$\approx$ 1, and high HSS) is the prediction whether or not CME will be strongly/intensly GCR-effective ($k < 2 \leftrightarrow FD < 3\,\%$), *i.e.* predicting whether CME will produce $FD > 3\,\%$.

6. Summary and conclusions

We used a sample of CME–flare pairs detected remotely, and the associated cosmic ray (CR) count levels at Earth for the purpose of forecasting the CME-associated Forbush decrease (FD) magnitude [FD]. The advantage of the approach is in the early forecast, since the travel time for a CME from Sun to Earth is of the order of $\approx$ one day. To characterize CME/flare event we use L1 coronagraphic CME observations, the EUV flare-position observation, as well as the soft X-ray flare measurements. We note that some of the properties derived from these observations can also be obtained from ground-based measurements (*e.g.* proxy of the CME speed can be obtained from solar Type-II radio bursts, flare position can be obtained by H α observations). Therefore, the remotely observed CME/flare properties are not necessarily spacecraft-dependent.

The relationship between FD magnitude at the Earth and remote observations of CMEs and associated solar flares is studied *via* statistical analysis. It was found that FD magnitude is larger for faster CMEs with larger apparent width, associated with stronger flares, originating close to the center of the solar disc and (possibly) involved in a CME–CME interaction. These relations are quantified through the change in the distribution of FD magnitude, which is mathematically reconstructed using the shifted geometric distribution. The reconstructed distributions are used to obtain a joint probability distribution for a certain CME/flare event, where we use the sample of 187 CME–flare–FD associations as an ensemble of possibilities for a certain event. The joint probability distribution for a certain CME/flare event behaves differently when different CME/flare properties are used as input, reflecting the behavior found by statistical analysis. However, distributions are always highly asymmetric with the greatest probability that CME will not be GCR-effective, which is the general behavior of CMEs (a large majority of CMEs will never reach the Earth and/or will not be very GCR-effective). Therefore, we impose empirically optimized

thresholds on the probability distribution to obtain the estimation of the GCR-effectiveness for a specific CME/flare event. In this way we obtain an empirical probabilistic model that uses selected remote solar observations of CME and associated solar flare as an input and gives expected FD magnitude range as an output.

Evaluation of the forecast method is performed on the training set (the sample of 187 CME–flare–FD associations used for the statistical analysis) and test set (independent sample of 42 CME–flare–FD associations). The evaluation revealed that the forecast is less reliable when it is more specific, due to difficulties in discerning between neighboring bins. It was found especially ineffective for prediction of intermediate FD magnitudes ($1\,\% < FD < 3\,\%$ and $3\,\% < FD < 6\,\%$). However, when the forecast is less specific, the quality of the forecast improves. Based on the performed evaluation, the Forbush-decrease prediction is found to be most reliable in predicting whether or not CME will produce $FD > 3\,\%$.

Based on the research presented in this study, an online application for the prediction of Forbush decrease magnitude based on the remote solar observations of CMEs and associated solar flares, "Forbush Decrease Forecast Tool (FDFT)" was developed and is publically availabale at oh.geof.unizg.hr/FDFT/fdft.php. The full training-set list, as well as the test set list are also available at the same webpage under "Documentation".

Acknowledgements This work has been supported in part by Croatian Science Foundation under the project 6212 "Solar and Stellar Variability". M. Dumbović and J. Čalogović acknowledge the support by the ESF project PoKRet.

Disclosure of Potential Conflicts of Interest

The authors declare that they have no conflicts of interest.

References

Belov, A.V.: 2009, Forbush effects and their connection with solar, interplanetary and geomagnetic phenomena. In: Gopalswamy, N., Webb, D.F. (eds.) *IAU Symp., Proceedings of the Int. Astron. Union, Cambridge Univ. Press, Cambridge, UK* **257**, 439. DOI. ADS.

Belov, A., Abunin, A., Abunina, M., Eroshenko, E., Oleneva, V., Yanke, V., Papaioannou, A., Mavromichalaki, H., Gopalswamy, N., Yashiro, S.: 2014, Coronal Mass Ejections and Non-recurrent Forbush Decreases. *Sol. Phys.* **289**, 3949. DOI. ADS.

Blanco, J.J., Catalán, E., Hidalgo, M.A., Medina, J., García, O., Rodríguez-Pacheco, J.: 2013, Observable Effects of Interplanetary Coronal Mass Ejections on Ground Level Neutron Monitor Count Rates. *Sol. Phys.* **284**, 167. DOI. ADS.

Cane, H.V.: 2000, Coronal Mass Ejections and Forbush Decreases. *Space Sci. Rev.* **93**, 55. DOI. ADS.

Cane, H.V., Richardson, I.G., Wibberenz, G.: 1995, The Response of Energetic Particles to the Presence of Ejecta Material. In: Iucci, N., Lamanna, E. (eds.) *24th Int. Cosmic Ray Conf., Rome, proceedings* **4**, 377. ADS.

Chertok, I.M., Grechnev, V.V., Belov, A.V., Abunin, A.A.: 2013, Magnetic Flux of EUV Arcade and Dimming Regions as a Relevant Parameter for Early Diagnostics of Solar Eruptions - Sources of Non-recurrent Geomagnetic Storms and Forbush Decreases. *Sol. Phys.* **282**, 175. DOI. ADS.

Chilingarian, A., Bostanjyan, N.: 2010, On the relation of the Forbush decreases detected by ASEC monitors during the 23rd solar activity cycle with ICME parameters. *Adv. Space Res.* **45**, 614. DOI. ADS.

Devos, A., Verbeeck, C., Robbrecht, E.: 2014, Verification of space weather forecasting at the Regional Warning Center in Belgium. *J. Space Weather Space Clim.* **4**(27), A29. DOI. ADS.

Dumbović, M., Vršnak, B., Čalogović, J., Karlica, M.: 2011, Cosmic ray modulation by solar wind disturbances. *Astron. Astrophys.* **531**, A91+. DOI. ADS.

Dumbović, M., Vršnak, B., Čalogović, J., Župan, R.: 2012, Cosmic ray modulation by different types of solar wind disturbances. *Astron. Astrophys.* **538**, A28. DOI. ADS.

Dumbović, M., Devos, A., Vršnak, B., Sudar, D., Rodriguez, L., Ruždjak, D., Leer, K., Vennerstrøm, S., Veronig, A.: 2015, Geoeffectiveness of Coronal Mass Ejections in the SOHO Era. *Sol. Phys.* **290**, 579. DOI. ADS.

Forbush, S.E.: 1937, On the effects in cosmic-ray intensity observed during the recent magnetic storm. *Phys. Rev.* **51**(12), 1108. DOI.

Hess, V.F., Demmelmair, A.: 1937, World-wide Effect in Cosmic Ray Intensity, as Observed during a Recent Magnetic Storm. *Nature* **140**, 316. DOI. ADS.

Howard, T.A., Harrison, R.A.: 2013, Stealth Coronal Mass Ejections: A Perspective. *Sol. Phys.* **285**, 269. DOI. ADS.

Jordan, A.P., Spence, H.E., Blake, J.B., Shaul, D.N.A.: 2011, Revisiting two-step Forbush decreases. *J. Geophys. Res.* **116**, 11103. DOI. ADS.

Krittinatham, W., Ruffolo, D.: 2009, Drift Orbits of Energetic Particles in an Interplanetary Magnetic Flux Rope. *Astrophys. J.* **704**, 831. DOI. ADS.

Kubo, Y., Shimazu, H.: 2010, Effect of Finite Larmor Radius on Cosmic-ray Penetration into an Interplanetary Magnetic Flux Rope. *Astrophys. J.* **720**, 853. DOI. ADS.

Kumar, A., Badruddin: 2014, Interplanetary Coronal Mass Ejections, Associated Features, and Transient Modulation of Galactic Cosmic Rays. *Sol. Phys.* **289**, 2177. DOI. ADS.

Le Roux, J.A., Potgieter, M.S.: 1991, The simulation of Forbush decreases with time-dependent cosmic-ray modulation models of varying complexity. *Astron. Astrophys.* **243**, 531. ADS.

Parker, E.N.: 1965, The passage of energetic charged particles through interplanetary space. *Planet. Space. Sci.* **13**, 9. DOI. ADS.

Richardson, I.G.: 2004, Energetic Particles and Corotating Interaction Regions in the Solar Wind. *Space Sci. Rev.* **111**, 267. DOI. ADS.

Richardson, I.G., Cane, H.V.: 2010, Near-Earth Interplanetary Coronal Mass Ejections During Solar Cycle 23 (1996 - 2009): Catalog and Summary of Properties. *Sol. Phys.* **264**, 189. DOI. ADS.

Richardson, I.G., Cane, H.V.: 2011, Galactic Cosmic Ray Intensity Response to Interplanetary Coronal Mass Ejections/Magnetic Clouds in 1995 - 2009. *Sol. Phys.* **270**, 609. DOI. ADS.

Robbrecht, E., Patsourakos, S., Vourlidas, A.: 2009, No Trace Left Behind: STEREO Observation of a Coronal Mass Ejection Without Low Coronal Signatures. *Astrophys. J.* **701**, 283. DOI. ADS.

Stirzaker, D.: 2003, *Elementary Probability*, Cambridge University Press, New York.

Sudar, D., Vršnak, B., Dumbović, M.: 2015, Predicting Coronal Mass Ejection transit time to Earth with neural network. *Mon. Not. R. Astron. Soc.*, submitted.

Thomas, S.R., Owens, M.J., Lockwood, M., Barnard, L., Scott, C.J.: 2015, Near-Earth Cosmic Ray Decreases Associated with Remote Coronal Mass Ejections. *Astrophys. J.* **801**, 5. DOI. ADS.

Uwamahoro, J., McKinnell, L.A., Habarulema, J.B.: 2012, Estimating the geoeffectiveness of halo CMEs from associated solar and IP parameters using neural networks. *Ann. Geophys.* **30**, 963. DOI. ADS.

Valach, F., Revallo, M., Bochníček, J., Hejda, P.: 2009, Solar energetic particle flux enhancement as a predictor of geomagnetic activity in a neural network-based model. *Space Weather* **7**, 4004. DOI. ADS.

Wibberenz, G., Cane, H.V., Richardson, I.G.: 1997, Two-step Forbush Decreases in thecInner Solar System and their Relevance for Models of Transient Disturbances. In: Potgieter, M.S., Raubenheimer, C., van der Walt, D.J. (eds.) *25th Int. Cosmic Ray Conf., Durban, proceedings* **1**, 397. ADS.

Wibberenz, G., Le Roux, J.A., Potgieter, M.S., Bieber, J.W.: 1998, Transient Effects and Disturbed Conditions. *Space Sci. Rev.* **83**, 309. ADS.

Yashiro, S., Gopalswamy, N., Michalek, G., St. Cyr, O.C., Plunkett, S.P., Rich, N.B., Howard, R.A.: 2004, A catalog of white light coronal mass ejections observed by the SOHO spacecraft. *J. Geophys. Res.* **109**, 7105. DOI. ADS.